Check for updates

Surface modified zinc ferrite as a carbon-alternative negative electrode for high-energy hybrid supercapacitor

Abhijeet V. Shinde [a], Swati J. Patil [b], Seung-Kyu Hwang [c], Ganji Seeta Rama Raju [b], Yun-Suk Huh [c,***], Young-Kyu Han [b,**], Nilesh R. Chodankar [b,*]

[a] *Shri Swami Vivekanand Shikshan Sanstha Vivakanand College, Tarabai Park, Kolhapur, 416 003, India*
[b] *Department of Energy and Materials Engineering, Dongguk University-Seoul, Seoul, 100-715, Republic of Korea*
[c] *Department of Biological Engineering, NanoBio High-Tech Materials Research Center, Inha University, 100 Inha-ro, Incheon, 22212, Republic of Korea*

A R T I C L E I N F O

Keywords:
Precursors
Zinc ferrite
Hybrid supercapacitors
Polymer gel electrolytes

A B S T R A C T

The limited energy storage capacities of carbon-based negative electrodes, which rely on conventional double layer charge storage mechanisms, have limited the electrochemical performances of hybrid supercapacitors (HSCs). The development of nanostructured redox-active materials that serve as alternatives to carbon-based negative electrodes is crucial to overcome the limitations of current HSCs. In this work, a coordination chemistry approach is utilized to tune the nanostructure of zinc ferrite thin films on flexible stainless steel (SS) foil by using several zinc salt precursors, including $ZnCl_2 \cdot 6H_2O$, $Zn(NO_3)_2 \cdot 6H_2O$, and $ZnSO_4 \cdot 6H_2O$, while using the same iron precursor ($FeCl_2 \cdot 4H_2O$). Materials prepared with the $ZnCl_2 \cdot 6H_2O$ metal salt form porous nanosheets with groundnut-like structures that exhibit maximum specific capacities of 544 mA h/g (454 F/g) at current density of 2.5 A/g. Redox-active solid-state HSCs are assembled by using zinc ferrite as a negative electrode, MnO_2 nanoflakes as a positive electrode, and a polymer gel as the electrolyte. The developed solid-state HSC cells show excellent performance as exemplified by a maximum specific capacitance of 123.8 F/g and an energy density of 55.72 Wh/kg, both of which are superior to those of conventional carbon-based symmetric and HSCs.

1. Introduction

Supercapacitors (SCs) with two dissimilar electrodes are called as hybrid supercapacitors (HSCs) and generally exhibit higher energy storage capacities than conventional symmetric SC cells. HSCs are conventionally assembled by using a redox-active positive electrode (for example MnO_2, Co_3O_4, NiO, etc.), a carbon-based negative electrode (for example activated carbon, carbon nanotubes, graphene, etc.), and either a liquid or a solid electrolyte [1,2]. Yet, the low energy storage capacities of carbon-based negative electrodes bound the electrochemical performances of HSC cells according to the following equation; $C_d = 1/C_p + 1/C_n$, where, C_d, C_p, and C_n are the respective capacitances of the HSC cell, the positive electrode, and the negative electrode [3]. Thus, developing new redox-active materials that can serve as alternatives to carbon-based materials used as negative electrodes are important for boosting the energy storage capacities of HSC cells. With this motivation, different redox-active negative electrodes, such as Fe_2O_3,

V_2O_5, and Bi_2O_3 among others, have been explored for applications in HSCs, but their energy storage capacities, potential windows, and cycling stabilities have yet to supplant conventional carbon-based negative electrodes [4] [–] [7].

Binary metal oxides have been broadly tested for utilization in HSCs because of their higher electrical conductivities and charge storage capacities versus conventional unitary metal oxides [8]. Most of the reported binary metal oxides works in the positive potential range with higher energy storing capacity [9,10]. Among the numerous binary metal oxides, metal ferrites are favored as negative electrodes for HSCs because of their huge theoretical capacitance, capacity to form complex ions in the electrolyte, spinel structure, and, most importantly, their ability to foster synergic effects among multivalence metal cations [11] [–] [13]. These materials form complex species that are relatively larger in size, granting vast surface areas to accommodate electrolyte ions and, thus, yielding improved material performances. A characteristic of $ZnFe_2O_4$ is that it has two different metal cations, Zn and Fe, with O as

---

anion. The cations occupy two different positions in a spinel structure, which are tetrahedral (Zn) and octahedral (Fe) sites along the face-centered cubic (FCC) lattice formed by O^{2-} cations. The use of bimetallic oxides in negative electrode materials could enhance both electrical conductivity, by two orders of magnitude, and electrochemical activity versus materials prepared with unitary metal oxides [14].

In this work, to address the limitations of conventional carbon-based HSCs, we developed a facile chemical process for preparing redox-active, negative zinc ferrite electrodes with various Zn-metal precursors on pliable stainless steel (SS) substrates. We established the influence of different Zn-metal precursors on the structures and morphologies of the resulting materials. Moreover, the influence of microstructure on the electrochemical properties of these materials was also studied. Three-electrode electrochemical measurements were performed in 1 M Na_2SO_4 electrolyte, while two-electrode electrochemical measurements were carried out by arranging HSC cells in polymer gel electrolytes. The assembled redox-active HSC cell works in the higher working voltage of 1.8 V with capacitance of 123.8 F/g at current density of 2 A/g.

2. Experimental section

2.1. Preparation of ZnFe₂O₄ electrodes

A simple chemical bath deposition (CBD) method was used to prepare ZnFe₂O₄ thin-film electrodes. Three different Zn-metal precursors, including $ZnCl_2 \cdot 6H_2O$, $Zn(NO_3)_2 \cdot 6H_2O$, and $ZnSO_4 \cdot 6H_2O$, were used to prepare ZnFe₂O₄. ZnFe₂O₄ prepared by $ZnCl_2 \cdot 6H_2O$, $Zn(NO_3)_2 \cdot 6H_2O$, and $ZnSO_4 \cdot 6H_2O$ are referred to as ZnC, ZnN, and ZnS, respectively. ZnC, ZnN, and ZnS were prepared by initially dissolving the precursors (i.e. $ZnCl_2 \cdot 6H_2O$, $Zn(NO_3)_2 \cdot 6H_2O$, or $ZnSO_4 \cdot 6H_2O$) at 0.05 M in 80 ml of deionized (DI) water in separate glass beakers under continuous sonication for 20 min. Then, 0.1 M $FeCl_2 \cdot 4H_2O$ and 0.3 M urea were added to the Zn precursor solution and the solution was bath sonicated for 15 min to obtain a final solution where the Fe and Zn precursor ions were homogeneously distributed. Furthermore, the solutions were heated to 90 °C and a well-cleaned and pliable SS substrate was submerged into each of the prepared solutions for 4 h. Then, the ZnC, ZnN, and ZnS thin-film samples were removed from the precursor solution, washed several times with DI water, and stored in a vacuum oven for 6 h at 60 °C. The thin-film samples were then annealed at 450 °C for 3 h to obtain uniform

and adherent ZnFe₂O₄ thin films, which were subsequently characterized by structural, morphological, and electrochemical analyses. The mass loading of the active materials on the SS substrates is in the range of 2.7–3.0 mg/cm².

2.2. Three-electrode electrochemical measurements

Three-electrode electrochemical measurements were conducted to determine the best electrode for application as HSC. Specifically, cyclic voltammetry (CV) and galvanostatic charge-discharge (GCD) measurements were performed in 1 M Na_2SO_4 electrolytes. The three-electrode setup employs the prepared electrode (area of 1 cm²) as the working electrode, platinum foil as the counter electrode, and a saturated calomel electrode (SCE) as the reference electrode. The electrochemical measurements were carried out on a Zive SP6 instrument.

2.3. Fabrication of redox-active solid-state HSC cells

To assemble an HSC cell, two different electrodes are required to have dissimilar working potential windows in the same electrolyte. The prepared ZnFe₂O₄ electrodes can operate in a negative potential window in Na_2SO_4 electrolytes and, thus, act as a negative electrode for HSCs. Among the various reported positive electrodes, MnO₂ shows excellent electrochemical behavior in Na_2SO_4 electrolytes. Here, MnO₂ nanoflakes were prepared on SS substrates by a simple CBD method, as reported in our previous article [15]. Redox-active solid-state HSC cells were arranged by using the top-performing ZnC as the negative electrode, MnO₂ as the positive electrode, and carboxymethyl cellulose-Na₂SO₄ (CMC-Na₂SO₄) gel as the electrolyte. Note that CMC-Na₂SO₄ acts as an electrolyte as well as a separator. The CMC-Na₂SO₄ gel electrolyte was prepared by a solution casting method as follows: Initially, 2 g of CMC powder and 2 g of Na₂SO₄ were dissolved in 20 ml of DI water under constant stirring at 70 °C for 60 min. The resulting solution was viscous and gel-like. This solution was subsequently painted onto the ZnC and MnO₂ electrodes, which were then dried in an oven at 60 °C to remove water from the gel electrolyte. After drying, the two coated electrodes were pressed against one another to form the solid-state HSC cell, which was used for electrochemical tests including CV, GCD, and impedance analysis.
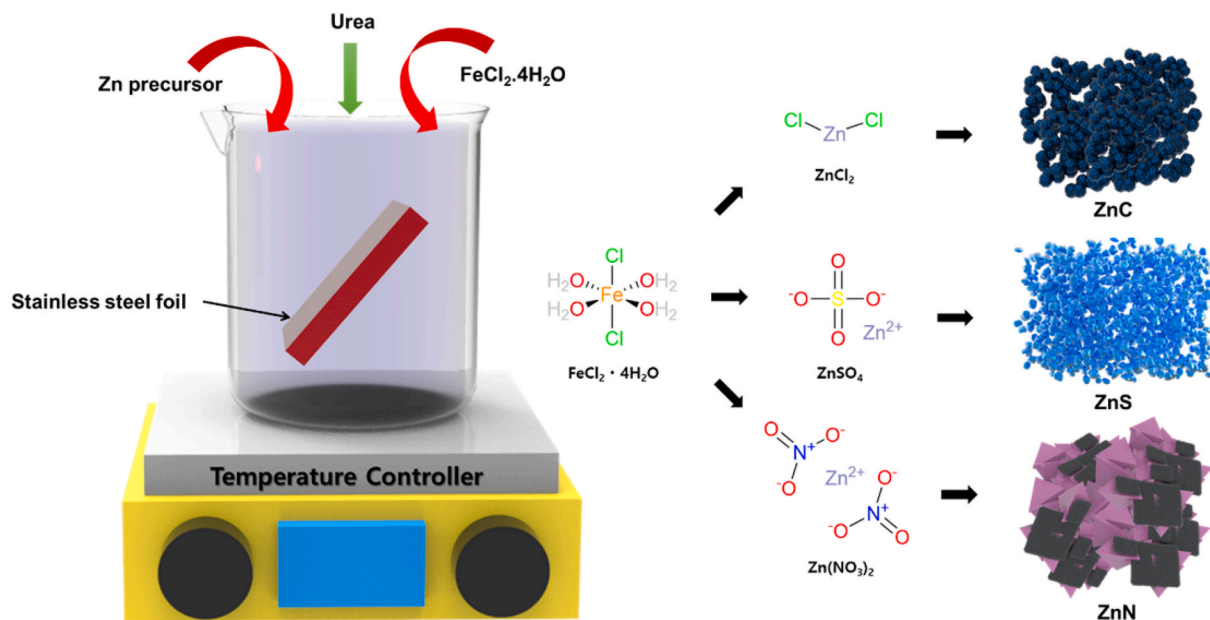
Fig. 1. Schematic of the methods used to prepare zinc ferrite thin-films on stainless steel substrates using different Zn metal precursors.
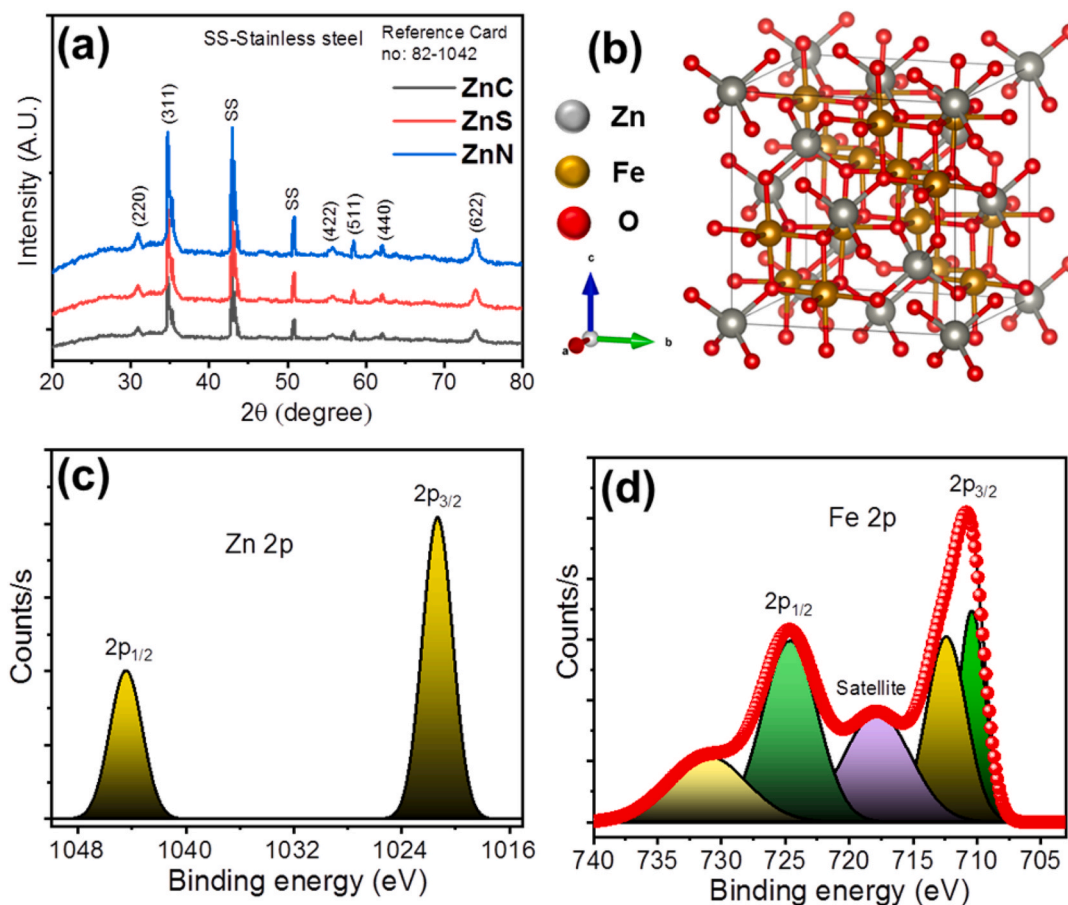
Fig. 2. (a) XRD patterns acquired from zinc ferrite materials prepared with different Zn metal precursors. (b) Crystallographic characteristics of ZnC, Narrow scan XPS spectra of the (c) Zn 2p and (d) Fe 2p of the ZnC sample.

3. Results and discussion

The negative electrode always presents obstacles for obtaining higher energy storing capacity in HSCs. Typically, carbon-based materials have been extensively used as negative electrodes for HSC applications as they can operate on the negative potential side in almost all types of electrolytes (acidic, basic, and neutral) [16]. However, the lower capacitance (100–200 F/g) of carbon-based electrodes, versus those of redox-active positive electrodes, limits the capacitance and energy density values of HSCs. To overcome this issue, we prepared redox-active zinc ferrite thin-films on pliable SS substrates by using a low-cost and binderless CBD method. A variety of Zn metal precursors were used to prepare $ZnFe_2O_4$ thin-films with nanostructures that promote greater energy storage capacities. According to Pearson's acid-base concept, metal ions and ligands are classified as either hard or soft [17]. Generally, hard acids favor binding to hard bases and vice-versa. In the present work, we used this concept to control the resulting nanostructures of the zinc ferrite thin-films. Specifically, we selected three different Zn^{2+} ion precursors, i.e. $ZnCl_2 \cdot 6H_2O$, $Zn(NO_3)_2 \cdot 6H_2O$, and $ZnSO_4 \cdot 6H_2O$, where Zn^{2+} is a hard acid and the basicity of the ligands follows the order $Cl^- > SO_4^{2-} > NO^{3-}$ [18]. Thus, Zn^{2+} binds more strongly to Cl^- than either SO_4^{2-} or NO^{3-}. This phenomenon defines both the reaction rates and the local concentration of Zn^{2+} ions, which, in turn, influence the particular size and shape of the final product on the SS substrate. Moreover, the complexing agent also plays an essential role in modifying the nanostructure at the surface of the thin-film. Here, urea is used as a complexing agent, the predominant role of which is to provide OH^- ions by thermal decomposition. Urea undergoes thermal decomposition during the reaction to produce hydroxide ions according to the following:

$$NH_2CoNH_2 + H_2O \rightarrow 2NH_3 + CO_2 \tag{1}$$

$$NH_3 + H_2O \leftrightarrow NH_4OH \tag{2}$$
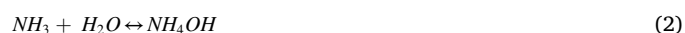
The resulting hydroxide species react with the Zn^{2+} ions to yield different architectures on the SS substrates. Lower reaction temperatures and chemical baths that are not stirred promote the slow release of Zn and Fe ions, which form hydroxide species according to the following reactions:

$$2FeCl_2 + 4OH^- \rightarrow 2FeOOH + 4Cl^- \tag{3}$$

$$ZnCl_2 + 2OH^- \rightarrow Zn(OH)_2 + 2Cl^- \tag{4}$$

$$ZnSO_4 + 2OH^- \rightarrow Zn(OH)_2 + 2SO_4^- \tag{5}$$

$$Zn(NO_3)_2 + 2OH^- \rightarrow Zn(OH)_2 + 2NO_3^- \tag{6}$$

$$Zn(OH)_2 + 2FeOOH \rightarrow ZnFe_2O_4 + 2H_2O \tag{7}$$
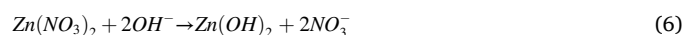
The Fe and Zn hydroxides react to form zinc ferrite on the SS substrate after thermal annealing at 450 °C. Fig. 1 shows the schematic procedure for preparing different nanostructured zinc ferrite samples on the SS substrates by using various Zn metal ion precursors. The structural features of the prepared zinc ferrite samples were investigated by X-ray diffraction (XRD) analyses, the results of which are presented in Fig. 2(a). The XRD patterns match well with the standard cubic spinal structure of zinc ferrite thin films, as defined by the standard JCPDS card no. 82–1042. As seen in the XRD patterns, there is no difference in the diffractions peaks for all zinc ferrite samples, except the peak intensities.
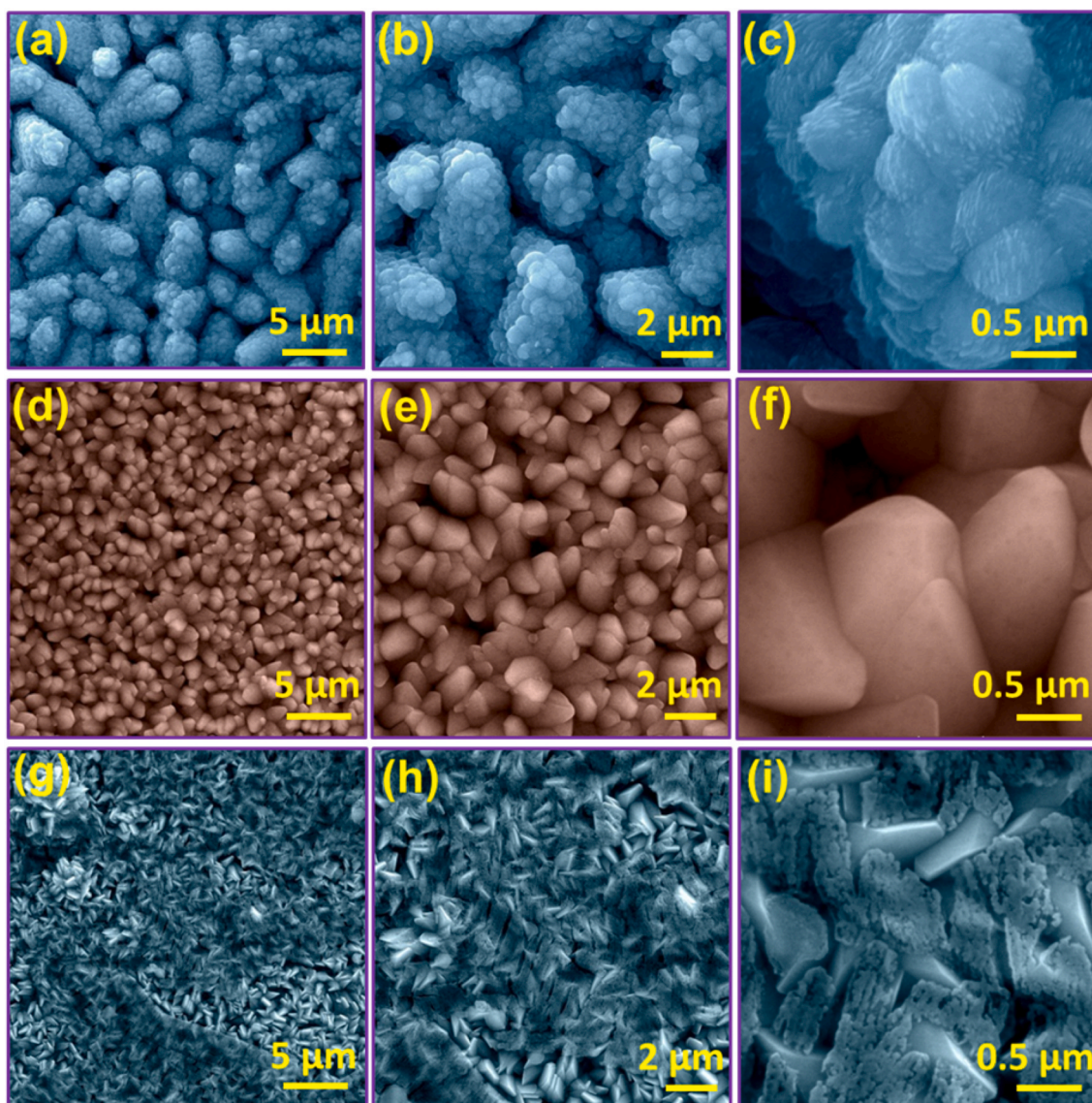
Fig. 3. SEM micrographs acquired from (a–c) ZnC, (d–f) ZnS, and (g–i) ZnN materials at three different magnifications.

The peak intensity for the diffraction peaks enhanced from the ZnC, ZnS to ZnN which indicates the ZnC has low crystalline nature than the ZnS and ZnN electrode materials. The broad and low intense diffraction peaks indicates nanocrystalline nature of ZnC. The broad peaks with low intensities of the ZnC sample are suitable for the energy storage purpose as it provides rapid ion diffusion in the active electrode material to enhance the resultant energy storing capacity [19,20]. Three-dimensional (3D) crystal structure of the ZnC sample is presented in Fig. 2(b). As seen in the figure, the Fe^{3+} is bonded to six equivalent O^{2-} atoms to form FeO_6 octahedra that share corners with six equivalent ZnO_4 tetrahedra and edges with six equivalent FeO_6 octahedra. Detailed characterization of the oxidation states and surface compositions of the ZnC thin films, which showed optimal electrochemical performance (see next section), were performed by X-ray photoelectron spectroscopy (XPS) analysis. The wide scan spectra of the ZnC thin film are shown in Fig. S2 in the supporting information. The narrow scan XPS spectrum of Zn 2p (Fig. 2(c)) shows two major peaks at binding energies of 1021.30 and 1044.41 eV that relate to Zn $2p_{3/2}$ and Zn $2p_{1/2}$, respectively. Furthermore, the spin-energy separation of Zn $2p_{3/2}$ and Zn $2p_{1/2}$ is 23.11 eV, confirming that Zn is in a +2 oxidation state [21]. Similarly, the narrow scan XPS spectrum of Fe 2p (Fig. 2(d)) displays two major contributions at 724.77 and 710.73 eV that originate from Fe $2p_{1/2}$ and

Fe $2p_{3/2}$, respectively. Moreover, the spin-energy separation of 14.04 eV shows that Fe is in a +3 oxidation state, as anticipated for a zinc ferrite thin film sample [22]. The narrow scan O 1s XPS spectrum for the binding energy range of 530–533 eV could be deconvoluted into three peaks (Supporting information, Fig. S2). The peak with the lowest binding energy (~530 eV) arises from the lattice oxygen species O^{2-}, while the remaining two peaks with greater binding energies originate from hydroxyl species (OH^-) or defective oxygen [23]. Further, XPS analyses reveal that the atomic percentages of Zn, Fe, O, and C are 9.22, 14.06, 48.9, and 27.82%, respectively.

The nanostructure at the surface is very important to SC performance because most of the electrochemical reactions occur at the surface [24]. [25] Scanning electron microscopy (SEM) was performed to interrogate the surface morphologies of various thin-film samples, the results of which are shown in Fig. 3. The SEM images of the ZnC sample reveal a porous groundnut-like structure (Fig. 3(a-c)). The surface of the groundnut-like structure is decorated with fine nanosheets, as observed in the magnified SEM image (Fig. 3(c)). The fine nanosheets and porous groundnut-like structures are favorable for SC applications as they provide large active sites for charge storage processes. The SEM images of ZnS demonstrate the formation of nanocones, with rigid surface characteristics (Fig. 3(d-f)), while randomly distributed nanobricks are
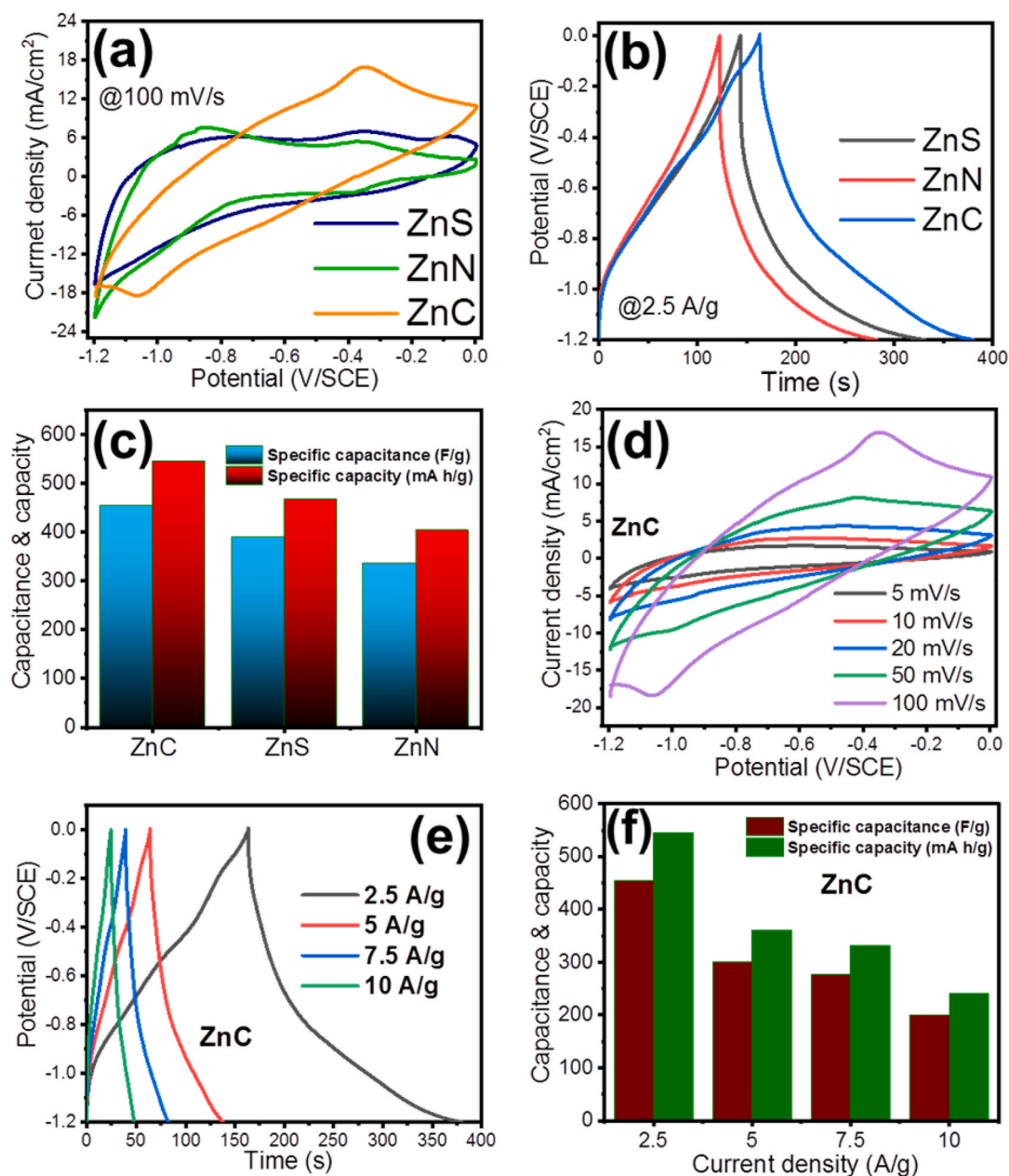
Fig. 4. Electrochemical behaviors of ZnC, ZnS, and ZnN electrodes in 1 M Na$_2$SO$_4$ electrolyte, including (a) CV and (b) GCD curves acquired at an identical scan rate (100 mV/s) and current density (2.5 A/g). (c) Plot of the specific capacitance and specific capacity of the ZnC, ZnS, and ZnN electrodes at a current density of 2.5 A/g. (d) CV and (e) GCD curves for the optimized ZnC electrode at various scan rates and current densities. (f)The specific capacity and specific capacity for the ZnC electrode at various current densities.

observed for the ZnN sample (Fig. 3(g-i)). Still, the nanosheets and porous groundnut-like structure of ZnC are more suitable for SCs because they provide more active sites for energy storage processes than the structures of the ZnS and ZnN samples. Moreover, water contact angle measurements (supporting information S3) show that ZnC has a lower water contact angle of 19° compared to ZnS (35°) and ZnN (63°). This significantly lower water contact angle of ZnC indicates that this electrode has higher surface energy compared to the ZnS and ZnN electrodes, which is favorable for interfacial electrochemical reactions between the electrode and electrolyte ions [26].

Three-electrode electrochemical measurements were performed to quantify the energy storage capacities of the prepared thin-film electrodes and to establish their potential applications in HSCs. The experiments used a traditional three-electrode setup where the thin-film electrode was used as the working electrode, a platinum plate as the

counter electrode, a saturated calomel electrode (SCE) as the reference electrode, and 1 M Na$_2$SO$_4$ in DI water as the electrolyte. Fig. 4(a) shows the CV curves measured for the various prepared electrodes at a scan rate of 100 mV/s over a performing potential window of −1.2 to 0.0 V/ SCE. A comparison of the CV curves reveals that the ZnC samples have greater energy storage capacities than the other electrodes. Moreover, similar trends emerged in the GCD curves, showing that the ZnC electrode exhibits higher charge and discharge times than the ZnS and ZnN electrodes. The GCD curves were used to calculate the specific capacity and capacitance of the various electrodes, and the results are illustrated in Fig. 4(c). At a current density of 2.5 A/g, ZnC, ZnS, and ZnN exhibit specific capacity values of 544, 467, and 403 mA h/g, respectively. The superior storage capacity of the ZnC electrode is attributed to its nanostructure, which consists of porous nanosheets, as well as its higher surface energy compared to ZnS and ZnN. The CV and GCD
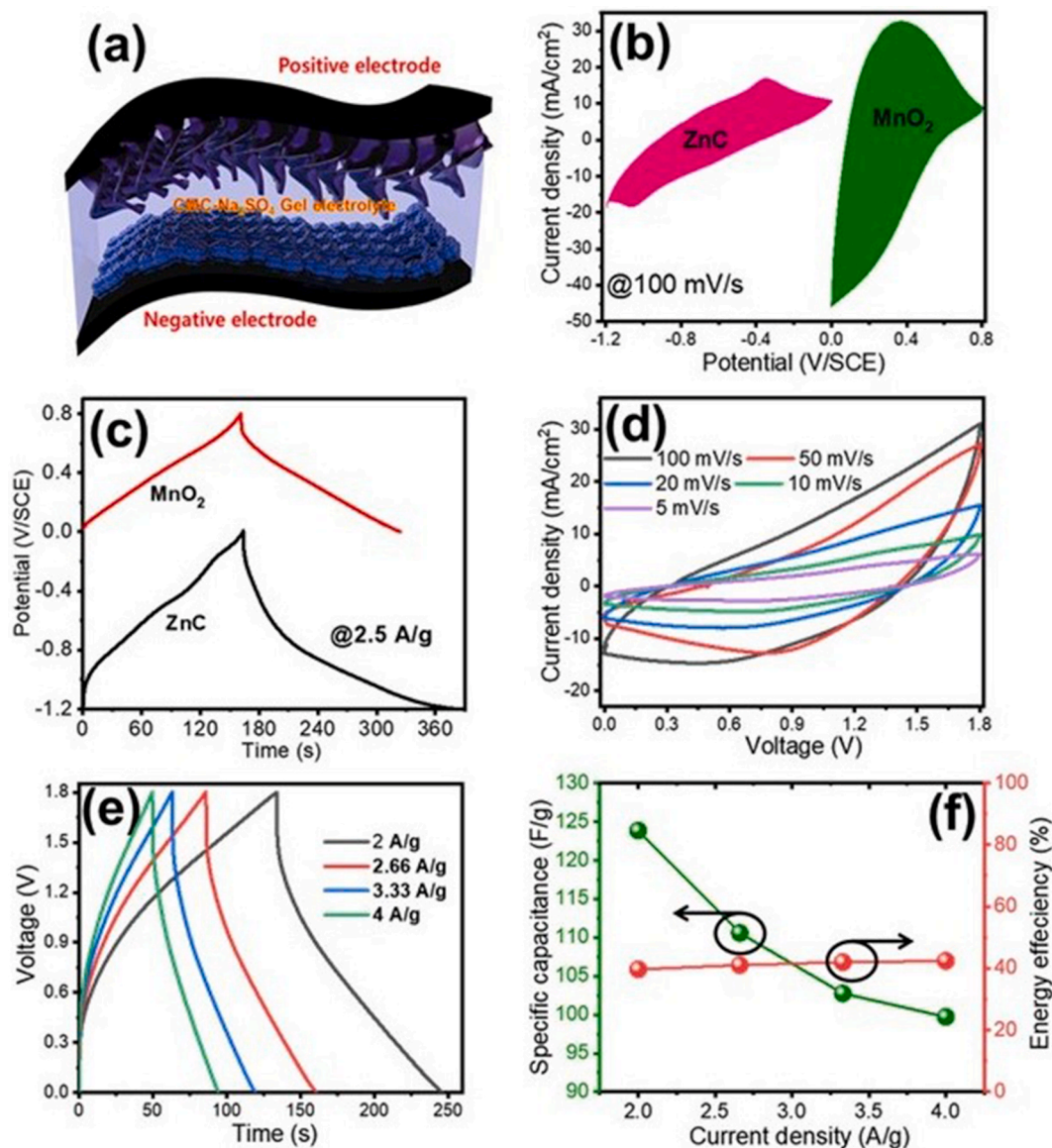
Fig. 5. (a) A schematic of the flexible MnO_2//ZnC HSC. (b) CV and (c) GCD curves for MnO_2 and ZnC electrodes in a three-electrode system with a 1 M Na_2SO_4 electrolyte. (d) CV and (e) GCD curves for anMnO_2//ZnC HSC at different scan rates and current densities over a voltage range of 0–1.8 V. (f) Plot of specific capacitance and energy efficiency of the MnO_2//ZnC HSC cell at various current densities.

measurements were performed at different scanning rates and current densities to examine the rate capabilities of the ZnC electrode. Fig. 4(d) displays the CV curves acquired from the ZnC electrode at various scanning rates. Moreover, a semi-rectangular shape, that establishes the redox activity of the electrode, is clearly observed. In addition, the area concealed by the CV curves increases with scan rate, indicating better rate capabilities for the ZnC electrode. Similarly, the GCD curves illustrate non-linear behaviors at all current densities, supporting the CV analyses (Fig. 4(e)). Fig. 4(f) shows a graph of the specific capacity versus the current density for the ZnC electrode. At a lower current density of 2.5 A/g, the electrode shows a maximum specific capacity of 544 mA h/g, which decreases to 240.4 mA h/g at a current density of 10 A/g with a rate capability of 44.19%. More importantly, however, the specific capacities and capacitance are much greater than previously reported for carbon-based SCs [27] [–] [30].

The excellent energy storage capacity of the ZnC electrodes, especially when compared to traditional carbon-based electrodes, encouraged the development of HSCs using the ZnC electrode [31] [–] [33]. The large working potential of the ZnC electrode on the negative side is

beneficial for enhancing the energy storage capacities of HSCs. As a further development of the HSC cell, we prepared fine MnO_2 nanosheets on a SS substrate as a positive electrode. A schematic of the assembled redox-active carbon-free HSC is presented in Fig. 5(a). Fig. 5(b) shows the CV curves for the MnO_2 and ZnC electrodes in the three-electrode setup at a constant scan rate of 100 mV/s. As shown in the figure, the MnO_2 and ZnC electrodes show excellent supercapacitive behaviors over different potential windows, which results in higher voltages for the HSC cell developed here. Similarly, the GCD curves for the positive and negative electrodes, at a constant current density, are presented in Fig. 5 (c). The charges on both electrodes must be balanced in order to obtain excellent energy storage capacities. In this study, charges were balanced by adjusting the mass proportion of positive to negative electrode. Specifically, it was found that the optimized mass proportion of positive to negative electrode is 1:1.5. The CV curves at various scan rates, over a voltage window of 0–1.8 V, for the MnO_2/ZnC HSC are presented in Fig. 5(d). The CV contours exhibit similar shapes at low and high scan rates without any redox peaks, thus demonstrating the outstanding supercapacitive behavior achievable by properly balancing the masses
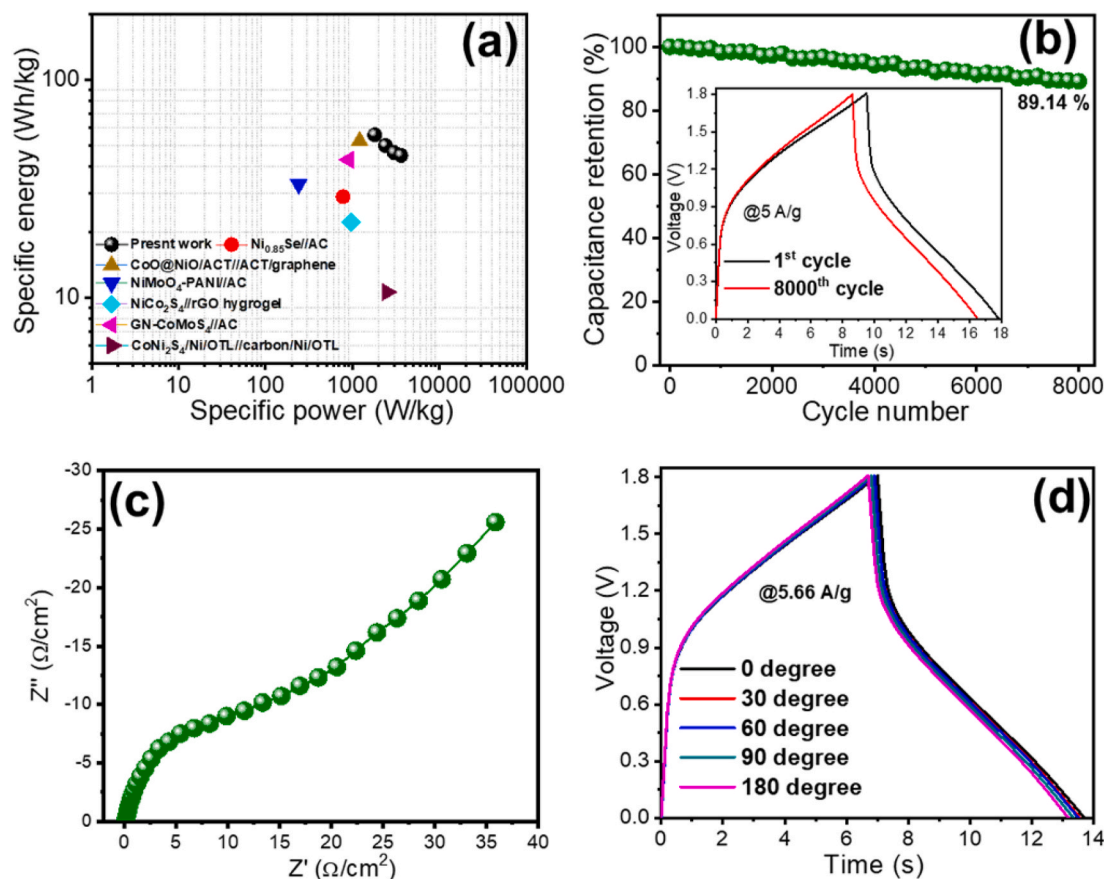
Fig. 6. (a) Ragone plot for the MnO_2//ZnC HSC and (b) a plot of capacitance retention versus cycle number for a MnO_2//ZnC HSC. The inset shows voltage for the 1st and 8000th GCD cycles. (c) Nyquist plot for the MnO_2//ZnC HSC. (d) The GCD curves for the MnO_2//ZnC HSC when bent at various angles at a current density of 5.66 A/g.

of the positive as well as negative electrode materials. Furthermore, the voltage window obtained for the MnO_2//ZnC HSC is higher than that of other widely studied HSC cells that employ Ni, Co, and carbon-based materials as electrodes [34] [–] [37]. Fig. 5(e) presents the GCD curves of the MnO_2//ZnC HSC at various current densities but in the same voltage window. No potential drops were observed, which implies excellent intercommunication between the gel electrolyte and the working electrode. Moreover, the non-linear behavior of the GCD curve demonstrates that both electrodes are redox-active. Analyses of the GCD curves for the MnO_2//ZnC HSC enables the calculation of the specific capacitance and energy efficiency at various current densities, which are presented in Fig. 5(f). This figure depicts that the HSC cell delivers a maximum specific capacitance of 123 F/g at a relatively low current density of 2 A/g, but a lower capacitance of 99 F/g at a higher current density of 4 A/g. The energy efficiency can be interpreted as the ratio of the discharging and charging energy densities, which is always less than one. Energy efficiency is especially important for energy storage systems, such as HSCs, because it serves as a figure of merit that defines the practical capabilities of the developed cells. Here, the MnO_2//ZnC HSC cell shows energy efficiencies that range from 40 to 50% depending on the current density.

The Ragone plot in Fig. 6(a) compares the MnO_2//ZnC HSC cell with other reported HSC cells that employ carbon-based materials as the negative electrode. The plot shows that the MnO_2//ZnC HSC cell exhibits a maximum specific energy of 55.72 Wh/kg at a specific power of 1800 W/kg and a specific energy of 44.87 Wh/kg at a higher specific power of 3600 W/kg. These results demonstrate that the MnO_2//ZnC HSC cell has a high energy storage capacity as well as the capability to operate at high powers. The specific energy of the MnO_2//ZnC HSC cell

is much higher than that previously reported for carbon-based HSCs [38] [–] [43]. In addition to the specific energy, the cycling stability of an HSC is of great importance for energy storage systems because higher cycling stabilities reduce maintenance costs. The plot in Fig. 6(b) illustrates the capacitance retention of the MnO_2//ZnC cell as it is cycled up to 8000 cycles at a high current density of 5 A/g. The cell shows an admirable capacitance retention of 89.14% after 8000 cycles, demonstrating the remarkable compatibility of the positive and negative electrodes with the gel electrolyte. The comparative table for the specific capacitance, specific energy, specific power and cycling stability for the HSC cells are provided in the supporting information SI 3. Deeper insights into the electrochemical interactions between the electrode materials and the gel electrolytes are gained by using electrochemical impedance spectroscopy (EIS) analyses. Fig. 6(c) shows the Nyquist plot for the MnO_2//ZnC HSC over a frequency range of 100 MHz to 100 kHz at a constant bias potential of 10 mV. As seen in the Nyquist plot, the semicircle in the high-frequency field corresponds to the charge transfer resistance (R_{ct}), which was 13.12 Ω/cm^2 for the MnO_2//ZnC HSC. Furthermore, the first cutoff of the Nyquist plot to the real axis indicates the equivalent series resistance (R_s), which was 4.2 Ω/cm^2 for the MnO_2/ZnC HSC cell. This suggests efficient contacts between the current collector, the active electrode materials, and the gel electrolyte. The relatively low R_s and R_{ct} values likely originate from the binder-free approach used to prepare the electrode materials and the painting of the gel electrolyte onto the positive and negative electrode materials, both of which minimize the contact resistance and enhance the electrochemical performances of the HSC cell. Flexibility tests were carried out by measuring the GCD curves for HSC cells that were bent at various angles, the results of which are plotted in Fig. 6(d). Moreover, the GCD

curves collected at different bending positions nearly overlap, reflecting that the performance of the MnO_2//ZnC HSC cell is retained even under mechanical stress. The excellent electrochemical features of the MnO_2//ZnC HSC cell is accredited to (i) the redox activities of the positive and negative electrodes that enhance the capacitance and energy density of the HSC cell, (ii) the binder-free preparation approach for both electrode materials to avoid unnecessary dead surface area and minimize the resulting resistance, (iii) the nanoporous surface architecture of the positive and negative electrode materials that provide large active sites to support energy storage processes, (iv) painting of the gel electrolyte onto the active electrode materials to avoids unnecessary resistances that are typically present in HSC or asymmetric cells where a gel electrolyte film is used as electrolyte, and (v) the gel electrolyte serving as both a separator and electrolyte to minimize the resistance that typically results from the separator.

4. Conclusions

In summary, we developed redox-active zinc ferrite thin-films for use as the negative electrodes in HSC cells to overcome the limitations of traditional carbon-based HSC cells. Simple coordination chemistry approaches were employed to optimize the nanostructure and Zn metal precursor of the zin ferrite electrodes. Specifically, the $ZnCl_2 \cdot 6H_2O$ metal salt precursor was used to form optimized zinc ferrite materials (called "ZnC") that consisted of nanosheets organized into groundnut-like nanostructured morphologies. Negative electrodes prepared from ZnC materials exhibited a maximum specific capacity of 544 mA h/g (454 F/g), which is superior to conventional carbon-based negative electrodes. Carbon-free redox-active solid-state HSCs with ZnC and MnO_2 nanosheets electrodes showed an excellent specific capacitance of 123 F/g in a high voltage window of 1.8 V. Moreover, the cell delivered a specific energy of 55.72 Wh/kg, which is significantly higher than that of conventional carbon-based asymmetric and hybrid SCs.

Declaration of competing interest

The authors declare that they have no known competing financial interests or personal relationships that could have appeared to influence the work reported in this paper.

Acknowledgements

Appendix A. Supplementary data

Supplementary data to this article can be found online at https://doi.org/10.1016/j.ceramint.2021.02.213.

References

[1] D.P. Dubal, N.R. Chodankar, D.H. Kim, P. Gomez-Romero, Towards flexible solid-state supercapacitors for smart and wearable electronics, Chem. Soc. Rev. 47 (2018) 2065–2129, https://doi.org/10.1039/c7cs00505a.

[2] N.R. Chodankar, H.D. Pham, A.K. Nanjundan, J.F.S. Fernando, K. Jayaramulu, D. Golberg, Y.K. Han, D.P. Dubal, True meaning of pseudocapacitors and their performance metrics: asymmetric versus hybrid supercapacitors, Small 16 (2020) 1–35, https://doi.org/10.1002/smll.202002806.

[3] S.J. Patil, N.R. Chodankar, Y.K. Han, D.W. Lee, Carbon alternative pseudocapacitive V_2O_5 nanobricks and δ-MnO_2 nanoflakes @ α-MnO_2 nanowires hetero-phase for high-energy pseudocapacitor, J. Power Sources 453 (2020) 227766, https://doi.org/10.1016/j.jpowsour.2020.227766.

[4] Y. Liu, D. Luo, K. Shi, X. Michaud, I. Zhitomirsky, Asymmetric supercapacitor based on MnO_2 and Fe_2O_3 nanotube active materials and graphene current collectors, Nano-Structures and Nano-Objects 15 (2018) 98–106, https://doi.org/10.1016/j.nanoso.2017.08.010.

[5] S.T. Senthilkumar, R. Kalai Selvan, M. Ulaganathan, J.S. Melo, Fabrication of Bi2O3||AC asymmetric supercapacitor with redox additive aqueous electrolyte and its improved electrochemical performances, Electrochim. Acta 115 (2014) 518–524, https://doi.org/10.1016/j.electacta.2013.10.199.

[6] P. Yang, Y. Ding, Z. Lin, Z. Chen, Y. Li, P. Qiang, M. Ebrahimi, W. Mai, C.P. Wong, Z.L. Wang, Low-cost high-performance solid-state asymmetric supercapacitors based on MnO2 nanowires and Fe2O3 Nanotubes, Nano Lett. 14 (2014) 731–736, https://doi.org/10.1021/nl404008e.

[7] X. Yu, J. Sun, W. Zhao, S. Zhao, H. Chen, K. Tao, Y. Hu, L. Han, MOF-derived Bi_2O_3@C microrods as negative electrodes for advanced asymmetric supercapacitors, RSC Adv. 10 (2020) 14107–14112, https://doi.org/10.1039/d0ra01470b.

[8] Z. Wu, Y. Zhu, X. Ji, NiCo2O4-based materials for electrochemical supercapacitors, J. Mater. Chem. 2 (2014) 14759–14772, https://doi.org/10.1039/c4ta02390k.

[9] Y. Li, X. Han, T. Yi, Y. He, X. Li, Review and prospect of NiCo2O4-based composite materials for supercapacitor electrodes, J. Energy Chem. 31 (2019) 54–78, https://doi.org/10.1016/j.jechem.2018.05.010.

[10] W. Chu, Z. Shi, Y. Hou, D. Ma, X. Bai, Y. Gao, N. Yang, Trifunctional of phosphorus-doped NiCo2O4 nanowire materials for asymmetric supercapacitor, oxygen evolution reaction, and hydrogen evolution reaction, ACS Appl. Mater. Interfaces 12 (2020) 2763–2772, https://doi.org/10.1021/acsami.9b13182.

[11] X. Wu, Z. Han, X. Zheng, S. Yao, X. Yang, T. Zhai, Core-shell structured Co3O4@NiCo2O4 electrodes grown on flexible carbon fibers with superior electrochemical properties, Nano Energy 31 (2017) 410–417, https://doi.org/10.1016/j.nanoen.2016.11.035.

[12] Q. Wang, X. Wang, J. Xu, X. Ouyang, X. Hou, D. Chen, R. Wang, G. Shen, Flexible coaxial-type fiber supercapacitor based on NiCo2O4 nanosheets electrodes, Nano Energy 8 (2014) 44–51, https://doi.org/10.1016/j.nanoen.2014.05.014.

[13] S. Nagamuthu, S. Vijayakumar, S.H. Lee, K.S. Ryu, Hybrid supercapacitor devices based on MnCo2O4 as the positive electrode and FeMn2O4 as the negative electrode, Appl. Surf. Sci. 390 (2016) 202–208, https://doi.org/10.1016/j.apsusc.2016.08.072.

[14] A. Shanmugavani, R.K. Selvan, Synthesis of ZnFe2O4 nanoparticles and their asymmetric configuration with Ni(OH)2 for a pseudocapacitor, RSC Adv. 4 (2014) 27022–27029, https://doi.org/10.1039/c4ra01793e.

[15] N.R. Chodankar, D.P. Dubal, G.S. Gund, C.D. Lokhande, A symmetric MnO2/MnO2 flexible solid state supercapacitor operating at 1.6 v with aqueous gel electrolyte, J. Energy Chem. 25 (2016), https://doi.org/10.1016/j.jechem.2016.01.020.

[16] Y. Shabangoli, M.S. Rahmanifar, A. Noori, M.F. El-Kady, R.B. Kaner, M.F. Mousavi, Nile blue functionalized graphene aerogel as a pseudocapacitive negative electrode material across the full pH range, ACS Nano 13 (2019) 12567–12576, https://doi.org/10.1021/acsnano.9b03351.

[17] D.V. Shinde, D.Y. Ahn, V.V. Jadhav, D.Y. Lee, N.K. Shrestha, J.K. Lee, H.Y. Lee, R.S. Mane, S.H. Han, A coordination chemistry approach for shape controlled synthesis of indium oxide nanostructures and their photoelectrochemical properties, J. Mater. Chem. 2 (2014) 5490–5498, https://doi.org/10.1039/c3ta15407f.

[18] S.B. Bandgar, M.M. Vadiyar, Y.C. Ling, J.Y. Chang, S.H. Han, A.V. Ghule, S.S. Kolekar, Metal precursor dependent synthesis of NiFe2O4 thin films for high-performance flexible symmetric supercapacitor, ACS Appl. Energy Mater. 1 (2018) 638–648, https://doi.org/10.1021/acsaem.7b00163.

[19] M. Liang, M. Zhao, H. Wang, Q. Zheng, X. Song, Superior cycling stability of a crystalline/amorphous Co3S4 core-shell heterostructure for aqueous hybrid supercapacitors, J. Mater. Chem. 6 (2018) 21350–21359, https://doi.org/10.1039/c8ta08135b.

[20] Q. Li, Y. Xu, S. Zheng, X. Guo, H. Xue, H. Pang, Recent progress in some amorphous materials for supercapacitors, Small 14 (2018) 1–19, https://doi.org/10.1002/smll.201800426.

[21] A.E. Reddy, T. Anitha, C.V.V. Muralee Gopi, I.K. Durga, H.J. Kim, Facile synthesis of hierarchical ZnMn2O4@ZnFe2O4 microspheres on nickel foam for high-performance supercapacitor applications, New J. Chem. 42 (2018) 2964–2969, https://doi.org/10.1039/c7nj04269h.

[22] L. Li, H. Bi, S. Gai, F. He, P. Gao, Y. Dai, X. Zhang, D. Yang, M. Zhang, P. Yang, Uniformly dispersed ZnFe2O4 nanoparticles on nitrogen-modified graphene for high-performance supercapacitor as electrode, Sci. Rep. 7 (2017) 1–12, https://doi.org/10.1038/srep43116.

[23] P. Mountapmbeme Kouotou, H. Vieker, Z.Y. Tian, P.H. Tchoua Ngamou, A. El Kasmi, A. Beyer, A. Gölzhäuser, K. Kohse-Höinghaus, Structure-activity relation of spinel-type Co-Fe oxides for low-temperature CO oxidation, Catal. Sci. Technol. 4 (2014) 3359–3367, https://doi.org/10.1039/c4cy00463a.

[24] S. Chen, W. Xing, J. Duan, X. Hu, S.Z. Qiao, Nanostructured morphology control for efficient supercapacitor electrodes, J. Mater. Chem. 1 (2013) 2941–2954, https://doi.org/10.1039/c2ta00627h.

[25] J. Jiang, Y. Zhang, P. Nie, G. Xu, M. Shi, J. Wang, Y. Wu, R. Fu, H. Dou, X. Zhang, Progress of nanostructured electrode materials for supercapacitors, Adv. Sustain. Syst. 2 (2018) 1–24, https://doi.org/10.1002/adsu.201700110.

[26] M.M. Vadiyar, S.C. Bhise, S.K. Patil, S.S. Kolekar, A.R. Shelke, N.G. Deshpande, J.Y. Chang, K.S. Ghule, A.V. Ghule, Contact angle measurements: a preliminary diagnostic tool for evaluating the performance of ZnFe2O4 nano-flake based supercapacitors, Chem. Commun. 52 (2016) 2557–2560, https://doi.org/10.1039/c5cc08373g.

[27] H. Yang, S. Ye, J. Zhou, T. Liang, Biomass-derived porous carbon materials for supercapacitor, Front. Chem. 7 (2019) 1–17, https://doi.org/10.3389/fchem.2019.00274.

[28] J. Phiri, J. Dou, T. Vuorinen, P.A.C. Gane, T.C. Maloney, Highly porous willow wood-derived activated carbon for high-performance supercapacitor electrodes, ACS Omega 4 (2019) 18108–18117, https://doi.org/10.1021/acsomega.9b01977.

[29] R. Dubey, V. Guruviah, Review of carbon-based electrode materials for supercapacitor energy storage, Ionics 25 (2019) 1419–1445, https://doi.org/10.1007/s11581-019-02874-0.

[30] A. Borenstein, O. Hanna, R. Attias, S. Luski, T. Brousse, D. Aurbach, Carbon-based composite materials for supercapacitor electrodes: a review, J. Mater. Chem. 5 (2017) 12653–12672, https://doi.org/10.1039/c7ta00863e.

[31] B. Zhao, D. Chen, X. Xiong, B. Song, R. Hu, Q. Zhang, B.H. Rainwater, G.H. Waller, D. Zhen, Y. Ding, Y. Chen, C. Qu, D. Dang, C.P. Wong, M. Liu, A high-energy, long cycle-life hybrid supercapacitor based on graphene composite electrodes, Energy Storage Mater. 7 (2017) 32–39, https://doi.org/10.1016/j.ensm.2016.11.010.

[32] K. Shree Kesavan, K. Surya, M.S. Michael, High powered hybrid supercapacitor with microporous activated carbon, Solid State Ionics 321 (2018) 15–22, https://doi.org/10.1016/j.ssi.2018.04.005.

[33] A. Muzaffar, M.B. Ahamed, K. Deshmukh, J. Thirumalai, A review on recent advances in hybrid supercapacitors: design, fabrication and applications, Renew. Sustain. Energy Rev. 101 (2019) 123–145, https://doi.org/10.1016/j.rser.2018.10.026.

[34] S.J. Patil, N.R. Chodankar, R.B. Pujari, Y.K. Han, D.W. Lee, Core-shell hetero-nanostructured 1D transition metal polyphosphates decorated 2D bimetallic layered double hydroxide for sustainable hybrid supercapacitor, J. Power Sources 466 (2020), 228286, https://doi.org/10.1016/j.jpowsour.2020.228286.

[35] S.J. Patil, J.H. Kim, D.W. Lee, Graphene-nanosheet wrapped cobalt sulphide as a binder free hybrid electrode for asymmetric solid-state supercapacitor, J. Power Sources 342 (2017) 652–665, https://doi.org/10.1016/j.jpowsour.2016.12.096.

[36] J. Fang, C. Kang, L. Fu, S. Wan, Q. Liu, Morphology tuned synthesis of battery-type NiCo2O4 for high performance hybrid supercapacitors, J. Alloys Compd. 804 (2019) 1–9, https://doi.org/10.1016/j.jallcom.2019.06.230.

[37] N.R. Chodankar, G.S. Rama Raju, B. Park, P.A. Shinde, S. Chan Jun, D.P. Dubal, Y.S. Huh, Y.K. Han, Potentiodynamic polarization assisted phosphorus-containing amorphous trimetal hydroxide nanofibers for highly efficient hybrid supercapacitors, J. Mater. Chem. 8 (2020) 5721–5733, https://doi.org/10.1039/c9ta13225b.

[38] A. Ye, Y. Sui, J. Qi, F. Wei, Y. He, Q. Meng, Y. Ren, Z. Sun, Self-supported Ni0.85Se nanosheets array on carbon fiber cloth for a high-performance asymmetric supercapacitor, J. Electron. Mater. 47 (2018) 7002–7010, https://doi.org/10.1007/s11664-018-6627-5.

[39] M. Wei, C. Wang, Y. Yao, S. Yu, W.H. Liao, J. Ren, R. Sun, C.P. Wong, Toward high-performance all-solid-state supercapacitors using facilely fabricated graphite nanosheet-supported CoMoS4 as electrode material, Chemical Engineering Journal 355 (2019) 891–900, https://doi.org/10.1016/j.cej.2018.08.223.

[40] J. Song, Y. Chen, K. Cao, Y. Lu, J.H. Xin, X. Tao, Fully controllable design and fabrication of three-dimensional lattice supercapacitors, ACS Appl. Mater. Interfaces 10 (2018) 39839–39850, https://doi.org/10.1021/acsami.8b15731.

[41] F. Lu, M. Zhou, K. Su, T. Ye, Y. Yang, T.D. Lam, Y. Bando, X. Wang, Enhancing capacitance of nickel cobalt chalcogenide via interface structural design, ACS Appl. Mater. Interfaces 11 (2019), https://doi.org/10.1021/acsami.8b19035, 2082–2092.

[42] Z. Gao, N. Song, X. Li, Microstructural design of hybrid CoO@NiO and graphene nano-architectures for flexible high performance supercapacitors, J. Mater. Chem. 3 (2015) 14833–14844, https://doi.org/10.1039/c5ta03057a.

[43] H. Gao, F. Wu, X. Wang, C. Hao, C. Ge, Preparation of NiMoO4-PANI core-shell nanocomposite for the high-performance all-solid-state asymmetric supercapacitor, Int. J. Hydrogen Energy 43 (2018) 18349–18362, https://doi.org/10.1016/j.ijhydene.2018.08.018.